Assessment, Cause Localization, and Mitigation for Small-Signal Stability Risks in Multi-Parallel Grid-Forming Converter Systems

Feifan Chen, *Member, IEEE*, Xiongfei Wang, *Fellow, IEEE*, Lennart Harnefors, *Fellow, IEEE*, Sei Zhen Khong, *Senior Member, IEEE*, Jarno Kukkola, Mikko Routimo, *Member, IEEE*, Liang Zhao, *Member, IEEE*, Dan Wang, *Member, IEEE*, Henrik Sandberg, *Fellow, IEEE*, Kin Cheong Sou, *Member, IEEE*, and Karl Henrik Johansson, *Fellow, IEEE*

***Abstract*—This article addresses small-signal stability issues for multi-parallel grid-forming converter systems based on a newly developed extended passivity theory. The proposed methods provide streamlined, decentralized stability conditions that cover the full frequency range with reduced conservativeness, serving as theoretical tools and practical guidelines for assessment, cause localization, and mitigation of small-signal instability risks in such systems. Numerical examples and experimental results are provided to verify the effectiveness of the proposed methods.**

***Index Terms*—Control design, grid-connected converters, grid-forming, power system, stability.**

NOMENCLATURE

N	Number of parallel converters
k_i	Rated power coefficient of the ith converter
L_{fi}	Filter inductance of the ith converter
Z_{Li}	Line impedance of the ith converter
$\mathbf{Y}_{Li}$	Admittance matrix of the ith converter at the orientation point
$u_{Li,d,q}$	d–q voltage of the ith orientation point
$i_{i,d,q}$	d–q terminal current of the ith orientation point
$\Delta\theta_i$	Angle difference between the ith local d-q frame and the PCC d-q frame
$Q_{i,\theta}$	Rotation matrix
$\mathbf{Y}_i$	Equivalent admittance of the ith converter considering the line impedance
$G_i(s)$	Current-loop transfer function of the ith converter.
V_g	Grid voltage
d_i	operating-point perturbation of the ith converter
E_{pcc}	PCC voltage
$\mathbf{Z}_g$	grid impedance (predominantly inductive).
ν	Input-feedforward passivity (IFP) index
ρ	Output-feedback passivity (OFP) index
ν_R	Rotated IFP index
ρ_R	Rotated extended OFP index
$R(\omega)$	Frequency-dependent weighting matrix for extended passivity definitions.
ω_L	Low/high frequency boundary.
ν_E	Unified IFP index (low-frequency using ν_R, high-frequency using ν).
ρ_E	Unified OFP index (low-frequency using ρ_R, high-frequency using ρ).

Received 2 January 2025; revised 9 July 2025; accepted 29 August 2025. Date of publication 4 September 2025; date of current version 23 October 2025. The work of Sei Zhen Khong was supported by the National Science and Technology Council of Taiwan under Grant 113-2222-E-110-002-MY3 and Grant 114-2218-E-007-011. Paper no. TSG-00009-2025. *(Corresponding author: Xiongfei Wang.)*

Feifan Chen, Liang Zhao, Henrik Sandberg, and Karl Henrik Johansson are with the School of Electrical Engineering and Computer Science, KTH Royal Institute of Technology, 10044 Stockholm, Sweden (e-mail: feifanc@kth.se; liazhao@kth.se; hsan@kth.se; kallej@kth.se).

Xiongfei Wang is with the Department of Electrical Engineering, Tsinghua University, Beijing 100084, China (e-mail: xiongfei@tsinghua.edu.cn).

Lennart Harnefors is with the ABB Corporate Research, 72226 Västerås, Sweden (e-mail: lennart.harnefors@se.abb.com).

Sei Zhen Khong and Kin Cheong Sou are with the Department of Electrical Engineering, National Sun Yat-sen University, Kaohsiung 804, Taiwan (e-mail: szkhong@mail.nsysu.edu.tw; sou12@mail.nsysu.edu.tw).

Jarno Kukkola and Mikko Routimo are with the ABB Oy Drives, 00380 Helsinki, Finland (e-mail: mikko.routimo@fi.abb.com; jarno.kukkola1@fi.abb.com).

Dan Wang is with the School of Robotics and Automation, Nanjing University, Suzhou 215163, China (e-mail: danwang@nju.edu.cn).

Color versions of one or more figures in this article are available at https://doi.org/10.1109/TSG.2025.3606195.

Digital Object Identifier 10.1109/TSG.2025.3606195

I. INTRODUCTION

AS GRID-FORMING (GFM) converters gradually replace synchronous generators in power systems [1], [2], [3], [4], the issue of small-signal instability induced by GFM converter systems attracts increasing attention in recent years [5], [6], [7]. These oscillations pose challenges and risks for power system security and reliability. There is, therefore, an urgent need for the analysis and mitigation of instability risks in multi-parallel GFM converter systems [8].

The risk of small-signal instability is generally evaluated by determining whether the system meets certain stability conditions [9]. The small-signal stability conditions can be defined in the frequency domain, following two main approaches: centralized methods [6], [10], [11] and decentralized methods [12], [13], [14]. Centralized methods, such as Bode plot analysis and generalized Nyquist criteria [15], can provide necessary and sufficient stability boundaries without conservatism. However, applying these methods requires detailed information from all converters and the grid, which makes

them hardly scalable for multi-converter systems. Additionally, centralized approaches necessitate iterations of analysis whenever there is a change in the converter systems and involve time-consuming processes [9], [16]. The centralized methods are also difficult to pinpoint the instability causes within the system. While participation factor analysis can theoretically identify the influencing factors of stability [17], the high computation load and sophisticated analysis procedure make the method hardly scalable for systems with large number of converters. Additionally, it is necessary to identify the critical eigen-locus and the corresponding critical frequency range before conducting participation analysis, which is not trivial in practical applications.

Decentralized methods have been developed to facilitate stability assessment for complex systems [9], [12], [13], [14]. These methods avoid the need for computing the closed-loop poles and zeros based on the models of overall systems. However, they tend to be more conservative, offering only sufficient conditions for stability [16]. One of the most commonly used methods is the passivity theory [12], which evaluates the (energy) dissipative characteristics of the converter, quantified using a passivity index. Ideally, when each converter is passive, the system will be stable. However, converters cannot be fully dissipative at low frequencies, particularly in the frequency range around the fundamental frequency of the system, due to their constant power characteristics [18]. The inherently non-dissipative behavior renders the passivity-based stability criterion unsuitable for stability assessment and system analysis at low frequencies [19].

To address the limitations of impedance passivity theory at low frequencies, other decentralized methods have recently been introduced [9], [16], [20], [21]. In [16], it is demonstrated that using a transfer function matrix between power dynamics (ΔP, ΔQ and derivatives of the polar components of the bus voltage ($\Delta\tilde{\omega}$, $\Delta\tilde{V}_n^d$), significantly reduces conservatism at low frequencies. However, this method is merely recommended for low-frequency dynamics of converters, while impedance-based passivity analysis is reserved for high frequencies. Consequently, this approach introduces a "mid-frequency" gap between the upper limit of low-frequency range (0.2 p.u. or lower) and the lower limit of the high-frequency range (around 0.7 p.u.) and it requires that no oscillation modes exist within this band, which hardly holds, since the complex voltage-power couplings and interactions in GFM converters are likely to occur in such mid-frequency range [22]. Additionally, these different dynamic representations complicate practical implementation.

In [20], the small gain theorem is applied at low frequencies and the impedance passivity theory at high frequencies, yet the stability conditions at low frequencies remain challenging to be met, especially with controllers that include integrators [19], as these can lead to excessive singular values (gains) of converter admittance. In [9], [13], impedance modeling is retained, with the small gain theorem used for low frequencies and the newly developed small-phase theory [23], [24] applied at high frequencies. Unlike [20], a weighting matrix called a multiplier [25], [26] is introduced to facilitate these analyses. Stability is evaluated by comparing the gain and phase on both the converter and grid sides at low and high frequencies. However, there are still several limitations when using small gain and small phase theories together. First, although promising, the application of small phase theory in power electronics systems still requires further development, as the impedance of power electronic devices often does not satisfy the sectorial condition [13]. This added complexity limits the straightforward applicability of small phase theory in practical scenarios. Second, the frequency ranges where small gain and small phase theories are applicable tend to be case-specific, meaning that decentralized stability conditions based on these theories must adapt to each system's unique characteristics. Ideally, however, a more universal decentralized stability criterion—similar to the Nyquist criterion—would be desirable. Such a criterion could serve as a standardized guideline for impedance reshaping and a consistent dynamics specification for converters to 'follow' directly, thereby reducing the need for frequent recalibration of stability criteria in response to changing system configurations. In [27], a decentralized stability criterion is proposed, similar to the passivity theory but incorporates multipliers. However, its focus is on frequency control (the low-frequency range) in complex power grids, with limited attention given to the dynamics of power electronic devices.

This work is a further development of our previous studies [19], [21]. In [19], we discuss the limitations of traditional passivity theory in converter–grid systems. In [21], we introduced an extended-passivity framework, whose stability-specification ability was validated only on a simple single-converter setup; the results therein cannot directly address stability issues in multi-converter systems. This article makes two key contributions. First, we extend the aforementioned framework to multi-converter configurations and develop a decentralized, passivity-based suite of stability conditions and design methods for risk assessment, instability localization, and mitigation. Second, we demonstrate the applicability of passivity theory across the entire frequency spectrum for system-level integration, in contrast to its traditional use solely for high-frequency control design. Thus, this work significantly extends the application of passivity theory in power-electronics-based power systems—from controller design at the control level in [19], through stability specification at the converter level in [21], to system-level integration in multi-parallel converter configurations.

The methods presented in this article offer several notable advantages over previous decentralized approaches [9], [13], [16]. First, this approach eliminates the need for multiple dynamic representations or analytical tools; it relies solely on impedance modeling and extended passivity theory to achieve full-frequency-range coverage. This provides a clear and *non-case-specific* boundary for identifying potential stability risks. Second, the causes of instability can be localized within any subsystem partition without requiring participation factor calculations. Finally, a fully decentralized system design methodology is proposed, enabling mitigation of small-signal oscillation risks without considering various interaction levels in the system. This includes avoiding the analysis of inner and outer loop

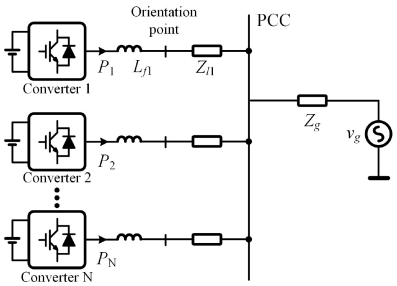

Fig. 1. Multi-parallel grid-connected converter system.

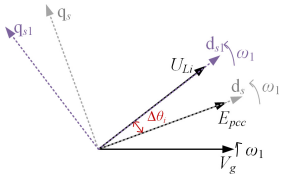

Fig. 2. An illustration of $\Delta\theta_i$.

couplings within each converter, interactions between different converters, and interactions between converters and the grid.

II. System Modeling

A. System Description and Impedance Modeling

In Fig. 1, all converters are connected to a common AC bus, considering the line impedance $\mathbf{Z}_{Li}$ between the orientation point of each converter and point of common coupling (PCC), where the subscript i represents the i-th converter. An output filter is placed at the output of each converter, and a constant DC voltage is assumed. On the grid side, an inductive-dominated grid impedance is assumed. The system is modeled in the per-unit (p.u.) system. Here, it is assumed that the voltage base value at the PCC is consistent with the grid voltage, set at 1.0 p.u. The rated transmission power on the common AC bus is defined as 1.0 p.u., implying that under rated conditions, the total transmission power of all converters sums up to 1 p.u. Consequently, in this p.u. system, the rated power of each converter is represented by a coefficient less than 1, denoted as k_i, and they satisfy $k_1 + k_2 + \cdots + k_N = 1$. Since each converter may have its own base values, when modeling the system, it is necessary to first convert the p.u. parameters of each converter based on its own base values to actual values, then calculate the p.u. values based on the system base values. Here, it is assumed that the admittances of all converters are modeled based on the system base values. The admittance matrix of the i-th converter obtained at its orientation point can be represented as

$$\begin{bmatrix} i_{i,d} \\ i_{i,q} \end{bmatrix} = \underbrace{\begin{bmatrix} Y_{Li,11} & Y_{Li,12} \\ Y_{Li,21} & Y_{Li,22} \end{bmatrix}}_{\mathbf{Y_{Li}}} \begin{bmatrix} u_{Li,d} \\ u_{Li,q} \end{bmatrix}, \tag{1}$$

where $i_{i,d}$ and $i_{i,q}$ are the d–q components of the converter's output current at its local orientation point, $u_{Li,d}$ and $u_{Li,q}$ are the corresponding d–q components of the voltage, and $\mathbf{Y}_{Li}$ denotes the converter's equivalent admittance matrix. For each element ($Y_{Li,mn}$) of the admittance matrix in (1), it is defined

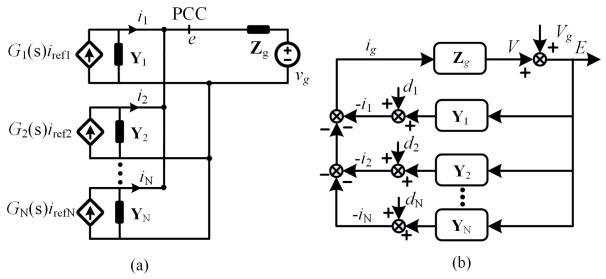

Fig. 3. (a) Equivalent circuit of multi-parallel grid-connected converter system. (b) Equivalent block diagram of multi-parallel grid-connected converter system.

in terms of the steady-state operating point, control structure, control parameters, and filter components shown in Fig. 1. The impedance-modeling methodology for converters with arbitrary control architectures is now mature; general derivation methods and expressions for the equivalent admittance of both PLL-synchronized and Power-synchronized converters have been derived in our previous work [28], [29], [30], [31]. Since the orientation points of each converter differ, and considering the presence of line impedance, these admittance matrices require further processing [32]. As shown in Fig. 2, d_{si} and q_{si} denote the d–q frame aligned with the ith converter's local orientation point, while d_s and q_s denote the common d–q frame aligned with the PCC voltage. There exists a phase shift $\Delta\theta_i$ between each individual converter's coordinate system and the common PCC-oriented frame. Therefore, to express all converter admittances in the PCC-oriented frame, we apply the rotation

$$\mathbf{Q}_{i,\theta} = \begin{bmatrix} \cos\Delta\theta_i & -\sin\Delta\theta_i \\ \sin\Delta\theta_i & \cos\Delta\theta_i \end{bmatrix}. \tag{2}$$

The equivalent admittance for i-th converter considering the line impedance from the PCC, is

$$\begin{bmatrix} i_{i,d} \\ i_{i,q} \end{bmatrix} = \underbrace{\begin{bmatrix} Y_{i,11} & Y_{i,12} \\ Y_{i,21} & Y_{i,22} \end{bmatrix}}_{\mathbf{Y}_i} \begin{bmatrix} u_d \\ u_q \end{bmatrix}. \tag{3}$$

Here, selecting the system coordinate system at the PCC as the reference coordinate system, each converter's admittance matrix, along with the incorporation of line impedance, yields the equivalent admittance $\mathbf{Y}_i$ as follows:

$$\mathbf{Y}_i = \mathbf{Q}_{i,\theta}^{-1}\left[\mathbf{Y}_{Li}^{-1} + \mathbf{Z}_{Li}\right]^{-1}\mathbf{Q}_{i,\theta}. \tag{4}$$

The system is equivalent to the circuit shown in Fig. 3(a), where G_i is the closed-loop transfer function of current control. The current source here serves to capture the steady-state operating point information. The transfer function G_i is inherently stable and acts as a low-pass filter, as shown in [18]. For example, for a proportional current controller with gain R_a, $G_i(s) = R_a/(R_a + sL)$, where L is the filter inductance. Here, G_i does not affect the stability assessment and is therefore approximated as unity.

B. Centralized Stability Condition

The current reference value variations of each converter and the disturbances in grid voltage are considered as inputs,

while the currents and PCC voltage are taken as the outputs. The equivalent block diagram corresponding to Fig. 3(a) is shown in Fig. 3(b), where V refers to the voltage drop across the grid impedance. When there are N parallel converters, it can be observed that this system has $N+1$ inputs and $N+1$ outputs. According to [33, Thm. 4.4],[1] the stability condition of this system is that the transfer function between any input and output does not have any right-half-plane poles or repeated poles on the imaginary axis. The input-output relation is characterized by

$$\begin{bmatrix} E_{pcc} \\ i_1 \\ \vdots \\ i_{\mathrm{N}} \end{bmatrix} = \begin{bmatrix} \mathbf{T}_{1,1} & \mathbf{T}_{1,2} & \cdots & \mathbf{T}_{1,\mathrm{N}+1} \\ \mathbf{T}_{2,1} & \mathbf{T}_{2,2} & \cdots & \mathbf{T}_{2,\mathrm{N}+1} \\ \vdots & \vdots & \ddots & \vdots \\ \mathbf{T}_{\mathrm{N}+1,1} & \mathbf{T}_{\mathrm{N}+1,2} & \cdots & \mathbf{T}_{\mathrm{N}+1,\mathrm{N}+1} \end{bmatrix} \begin{bmatrix} V_g \\ d_1 \\ \vdots \\ d_{\mathrm{N}} \end{bmatrix} \tag{5}$$

where d_i denotes the small-signal disturbance around the steady-state operating point, V_g is the grid-voltage disturbance input, and $\mathbf{T}_{m,n}$ is the transfer-function matrix mapping the nth disturbance to the mth output.

Therefore, to ensure system stability, it is necessary to check the stability of $(N+1)\times(N+1)$ transfer functions, which is impractical in practice when N is large. Assuming there is no pole-zero cancellation between the equivalent impedance $\mathbf{Y}_i$ of each converter and the grid impedance $\mathbf{Z}_g$, the stability condition can be significantly simplified [33]. It is sufficient to check the stability of any single transfer function in (5). Take $\mathbf{T}_{1,1}$, which is the closed-loop transfer function matrix from grid voltage disturbance to PCC voltage variation, as an example. The expression is given as

$$\mathbf{T}_{1,1} = \left[\mathbf{I} + \mathbf{Z}_g\left(\sum_{i=1}^{\mathrm{N}} \mathbf{Y}_i\right)\right]^{-1}. \tag{6}$$

Therefore, the system is stable if and only if (6) does not have right-half-plane poles or repeated poles on the imaginary axis, which is equivalent to the absence of right-half-plane zeros and repeated zeros on the imaginary axis in

$$\det\left[\mathbf{I} + \mathbf{Z}_g\left(\sum_{i=1}^{\mathrm{N}} \mathbf{Y}_i\right)\right]. \tag{7}$$

Since the grid impedance consists of passive components, and (7) is equal to

$$\det(\mathbf{Z}_g)\det\left[\mathbf{Z}_g^{-1} + \left(\sum_{i=1}^{\mathrm{N}} \mathbf{Y}_i\right)\right], \tag{8}$$

the stability of the system can also be determined by checking whether there are any right-half-plane zeros or repeated zeros on the imaginary axis in

$$\det\left[\mathbf{Z}_g^{-1} + \left(\sum_{i=1}^{\mathrm{N}} \mathbf{Y}_i\right)\right]. \tag{9}$$

[1][33, Thm. 4.4]: Given a negative feedback interconnection of G and K satisfying $y = d_y + Gu$, $u = d_u - Ky$ and denoted as $[G, K]$, where u and y are the system inputs and d_u and d_y are the disturbance signals, the feedback system is *internally stable* if and only if all four closed-loop transfer matrices in $u = (I+KG)^{-1}d_u - K(I+GK)^{-1}d_y$, and $y = G(I+KG)^{-1}d_u + (I+GK)^{-1}d_y$ are stable.

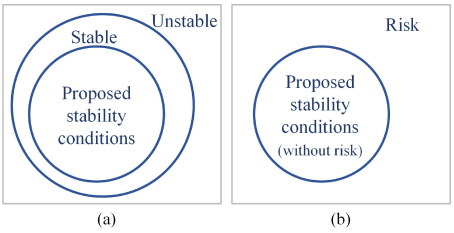

Fig. 4. Relationships between stability and risk. (a) The proposed stability condition is a sufficient condition for system stability. (b) If the system does not satisfy the proposed stability condition, it is considered to be at risk, and the system may be either stable or unstable.

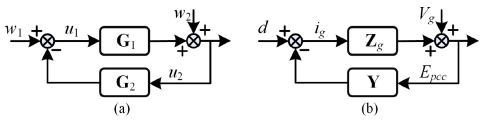

Fig. 5. Interconnected feedback system of (a) $[\mathbf{G}_1, \mathbf{G}_2]$. (b) $[\mathbf{Z}_g, \mathbf{Y}]$.

III. Theoretical Foundation of Decentralized Risk Assessment: A Passivity-Based Approach

The purpose of this section is to propose a decentralized stability condition for multi-parallel GFM converter systems. The relationship between system risk and system stability is illustrated in Fig. 4. The Venn diagram in Fig. 4 shows the relationship between system risk, the proposed decentralized stability condition, and overall system stability. Generally, a decentralized stability condition is a sufficient condition for system stability, as shown in Fig. 4(a). Therefore, when the system satisfies this condition, it is guaranteed to be stable. However, when the system does not meet this stability condition, it may be either stable or unstable, and is thus considered to be at risk, as shown in Fig. 4(b).

A. Preliminaries

According to [34], for a multi-input-multi-output (MIMO) system $\mathbf{G}$, its input feedforward passivity (IFP) index at frequency ω, denoted as $\nu[\mathbf{G}(s), \omega]$, is defined as

$$\frac{1}{2}\min\lambda\left[\mathbf{G}(j\omega) + \mathbf{G}^H(j\omega)\right], \tag{10}$$

and the output feedback passivity (OFP) index at frequency ω, denoted as $\rho[\mathbf{G}(s), \omega]$, is defined as

$$\frac{1}{2}\min\lambda\left(\mathbf{G}^{-1}(j\omega) + \mathbf{G}^{-H}(j\omega)\right), \tag{11}$$

where min λ is the minimum eigenvalue and the superscript H is the Hermitian operator, i.e., transpose–conjugate. For a general MIMO interconnected negative-feedback system $[\mathbf{G}_1, \mathbf{G}_2]$ shown in Fig. 5(a), the feedback system is stable when the open-loop systems satisfy the condition that

$$\nu[\mathbf{G}_1(s), \omega] + \rho[\mathbf{G}_2(s), \omega] > 0, \forall\omega \in [0, \quad +\infty]. \tag{12}$$

B. Extended Passivity Theory

In [21], we extend the definition of passivity index. For a MIMO system $\mathbf{G}$, its extended input feedforward passivity (IFP) index at frequency ω, denoted as $\nu_R[\mathbf{G}(s), \omega]$, is

defined as

$$\frac{1}{2}\min\lambda\Big[\mathbf{R}^H(\omega)\mathbf{G}(j\omega)+\mathbf{G}^H(j\omega)\mathbf{R}(\omega)\Big], \tag{13}$$

and the extended output feedback passivity (OFP) index at frequency ω, denoted as $\rho_R[\mathbf{G}(s),\omega]$, is defined as

$$\frac{1}{2}\min\lambda\Big[\mathbf{R}^H(\omega)\mathbf{G}^{-1}(j\omega)+\mathbf{G}^{-H}(j\omega)\mathbf{R}(\omega)\Big], \tag{14}$$

where the matrix $\mathbf{R}(\omega)$ is used to weight the system $\mathbf{G}$. For a general MIMO interconnected negative-feedback system [$\mathbf{G}_1$, $\mathbf{G}_2$] shown in Fig. 5(a), the feedback system is stable when the open-loop systems satisfy the condition that

$$\nu_R[\mathbf{G}_1(s),\omega]+\rho_R[\mathbf{G}_2(s),\omega]>0,\forall\omega\in[0,\ \ +\infty]. \tag{15}$$

It should be noted that when $\mathbf{R}(\omega)$ is the identity matrix, the definition of the index is consistent with the conventional passivity index definitions in (10) and (11). In this case, the stability condition provided in (15) represents the simplest version. A discussion on more general stability conditions, considering the use of different weight matrices across frequency bands, based on extended passivity theory, is provided in [21].

C. Definition of Unified Passivity Index

The system in Fig. 3 can be represented in the form of a negative feedback interconnected system, as shown in Fig. 5(b), denoted as [$\mathbf{Z}_g$, $\mathbf{Y}$], where $\mathbf{Y}=[\sum_{i=1}^{N}\mathbf{Y}_i]$. According to [21], the system is stable if it satisfies the following condition:

$$\nu_R(\mathbf{Y}(s),\omega)+\rho_R\big(\mathbf{Z}_g(s),\omega\big)>0,\ \ \forall\omega\in[0,\ \ +\infty]. \tag{16}$$

As in [21], the entire frequency range can be divided into several sub-bands, with different weight matrices used for each sub-band. As long as the sum of the indices for the converters and the grid at each frequency band is positive, the feedback system will be stable. Here, the frequency range is divided into two bands: the low-frequency band $[0,\omega_L)$ and the high-frequency band $[\omega_L,\infty]$, where $\omega_L\le 1.0$ p.u. In the range $[0,\omega_L)$, $\mathbf{R}$ is chosen as

$$\mathbf{R}=\begin{bmatrix}\cos\left(\frac{\pi}{2}\right) & \sin\left(\frac{\pi}{2}\right)\\ -\sin\left(\frac{\pi}{2}\right) & \cos\left(\frac{\pi}{2}\right)\end{bmatrix}=\begin{bmatrix}0 & 1\\ -1 & 0\end{bmatrix}, \tag{17}$$

while in the high-frequency band, the identity matrix is used. We justify below the choice of $\mathbf{R}$ in (17) from the perspective of $\mathbf{Z}_g$. Consider an inductive grid impedance $\mathbf{Z}_g$; in the d–q frame, its complex representation is $\mathbf{Z}_g=(s+j\omega_1)L_g$. By itself, this expression does not contribute any positive passivity index, while the converter's index at low frequencies remains negative, so passivity theory cannot be used for stability specification in that band. However, if we choose to rotate the term by $-90°$, i.e., multiply by $-j$, then $-j\,\mathbf{Z}_g=(\omega_1-js)\,L_g$. Here, the original $\omega_1 L_g$ term, which appeared in the imaginary part, now appears as a positive real part. This means that the rotated $\mathbf{Z}_g$ can provide a positive passivity index, which can be used to compensate for the converter's negative index.

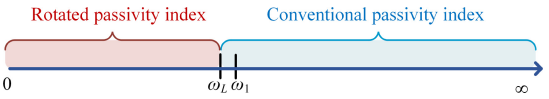

Fig. 6. Frequency range diagram of rotated passivity index and conventional passivity index.

In this article, within the frequency range $[0,\omega_L)$, the passivity index is referred to as the *rotated passivity index*, while in the high-frequency band $[\omega_L,\infty]$, it is referred to as the conventional passivity index. Based on the selection of the weighting matrix in (17), the value of ω_L is not fixed but may range from 0 to ω_1. The composition diagram of the unified passivity index is shown in Fig. 6. In all following examples in this article, ω_L is selected as ω_1, which is the base frequency (100π). To streamline discussion and prevent confusion, this article unifies the definitions of the rotated passivity index for the low-frequency band and the conventional passivity index for the high-frequency band. The resulting unified IFP index for the converter, denoted as ν_E, is defined as

$$\nu_E(\mathbf{Y}(s),\omega)=\begin{cases}\nu_R(\mathbf{Y}(s),\omega), & \forall\omega\in[0,\ \ \omega_L),\\ \nu(\mathbf{Y}(s),\omega), & \forall\omega\in[\omega_L,\ \ +\infty].\end{cases} \tag{18}$$

The unified OFP index for the grid side, denoted as ρ_E, is defined as

$$\rho_E\big(\mathbf{Z}_g(s),\omega\big)=\begin{cases}\rho_R\big(\mathbf{Z}_g(s),\omega\big), & \forall\omega\in[0,\ \ \omega_L),\\ \rho\big(\mathbf{Z}_g(s),\omega\big), & \forall\omega\in[\omega_L,\ \ +\infty].\end{cases} \tag{19}$$

Note: Although we refer to ν_E and ρ_E as "unified" indices, each is in fact defined piecewise in frequency (cf. (18)–(19)). Specifically, for $\omega<\omega_L$ they reduce to the weighted (rotated) indices ν_R and ρ_R, while for $\omega\ge\omega_L$ to the original indices ν and ρ. We adopt the unified symbols ν_E,ρ_E merely to streamline the presentation across the full spectrum.

D. Decentralized Stability Conditions for Risk Assessment

According to [21], the stability conditions for multi-parallel converter systems based on the extended passivity theory can be obtained as

$$\nu_E(\mathbf{Y}(s),\omega)+\rho_E\big(\mathbf{Z}_g(s),\omega\big)>0,\ \ \forall\omega\in[0,\ \ +\infty]. \tag{20}$$

Compared to condition (9), condition (20) allows information from the converter side and the grid impedance side to be calculated separately. However, the admittance of each converter needs to be summed up before the minimum eigenvalue is computed, which is computationally undesirable and not scalable. According to Weyl's inequality [33], a bound on the minimum index value of the aggregated admittance $\mathbf{Y}(s)$ by using the individual admittances $\mathbf{Y}_i(s)$ of each converter can be provided. Weyl's inequality states that the minimum eigenvalue of a sum of Hermitian matrices is at least the sum of their individual minimum eigenvalues. Hence, the following relationship holds:

$$\nu_E(\mathbf{Y}(s),\omega)\ge\sum_{i=1}^{N}\nu_E(\mathbf{Y}_i(s),\omega). \tag{21}$$

The relation in (21) further decentralizes the stability condition in (20) by breaking it into a summation of individual converter

contributions, a more decentralized version of the stability condition is obtained as

$$\sum_{i=1}^{N} \nu_E(\mathbf{Y}_i(s), \omega) + \rho_E\big(\mathbf{Z}_{\mathrm{g}}(s), \omega\big) > 0, \ \forall \omega \in [0, \ +\infty]. \quad (22)$$

It should be noted that this substitution comes with a trade-off in conservatism. However, this is evidently a scalable condition given that the number on the left-hand side can be reused for certifying system stability should a new converter connect to the grid. After obtaining the stability condition, the system's risk can be evaluated in a decentralized manner by comparing the converter-side index with the grid-side index, without the need to calculate closed-loop poles and zeros or plot Nyquist curves. Also, the index of any individual converter can be determined not only through analytical calculations but also through actual measurements. As shown in (13), once the impedance information at a specific frequency point is obtained via frequency scanning, the index can be derived by simply substituting the measured impedance into (13), requiring only an additional computation step. Therefore, this approach is applicable even in practical industrial scenarios where the analytical model cannot be directly obtained.

IV. A Passivity-Based Method for Risk Cause Localization

When a multi-converter system is in operation, it is essential to conduct a risk assessment for a specific converter or groups of converters, especially when the system includes devices from different manufacturers [35]. Identifying potential weak points quantitatively within the system is crucial. This section introduces a passivity-based approach for risk cause localization.

A. Stability Conditions for Different Subsystem Partitioning

If the entire system is considered as a whole without partitioning into subsystems, the equivalent admittance $\mathbf{Y}_{\mathrm{sys}}$ of the system is

$$\mathbf{Y}_{\mathrm{sys}} = \mathbf{Z}_g^{-1} + \left(\sum_{i=1}^{N} \mathbf{Y}_i\right). \quad (23)$$

To ensure system stability, it is sufficient to meet the following condition according to [36], [37]

$$\nu_E\left[\mathbf{Z}_g^{-1} + \left(\sum_{i=1}^{N} \mathbf{Y}_i\right), \omega\right] > 0, \ \forall \omega \in [0, \ +\infty]. \quad (24)$$

However, if one's interest lies in a specific part of the system, partitioning the system becomes necessary. In a system with N converters, the system can be partitioned into up to $N+1$ subsystems, including N subsystems for each converter and one subsystem for the grid impedance. More generally, if the number of partitioned subsystems is M, where M ranges from 1 to $N+1$, the corresponding stability criterion is

$$\sum_{i=1}^{M} \nu_E\big(\mathbf{Y}_{\mathrm{sub\_}i}(s), \omega\big) > 0, \ \forall \omega \in [0, \ +\infty]. \quad (25)$$

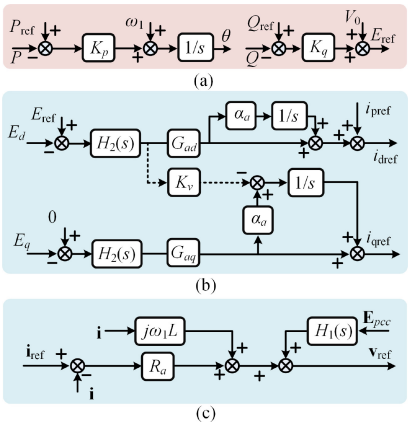

Fig. 7. GFM control within universal grid-connected converter control architecture proposed in [38].

According to Weyl's inequality [33], the stability condition derived for the entire system as a whole, shown in (24), is the least conservative. In contrast, the stability condition derived by dividing the system into $N+1$ subsystems, shown in (22), is the most conservative. The stability condition (25) occupies the middle ground. In practice, how to partition the subsystems varies case-by-case and is not the focus of this article. Therefore, this will not be discussed further. When using the proposed system diagnosis and converter risk assessment method, it is assumed that the system has already been partitioned into several subsystems.

B. Risk Cause Localization

For M subsystems, if the sum of their indices satisfies the conditions in (25), the system is considered stable. If (25) is not met within a specific frequency band, this does not necessarily indicate system instability but does suggest a potential risk. The passivity index values can be utilized to assess the risk level and identify high-risk subsystems.

The specific steps are summarized as follows:

Step 1: Partition the system into subsystems based on the actual situation.

Step 2: Obtain the unified passivity index plot for each subsystem through measurements or analytical methods.

Step 3: Plot the sum of the passivity indices of the subsystems.

Step 4: Identify the frequency bands where the sum of the passivity indices is negative.

Step 5: Find the subsystem with the minimum passivity index in these frequency bands and redesign it to reduce the risk.

Step 6: If a specific converter needs to be pinpointed, a more precise localization can be achieved by analyzing the passivity index of each converter within the highest risk subsystem.

C. Case Study

The GFM control used in this article is shown in Fig. 7, which is same as [38]. Using a three-converter system as an example, the system is divided into two subsystems: Subsystem 1 consists of converters 1 and 2, while Subsystem

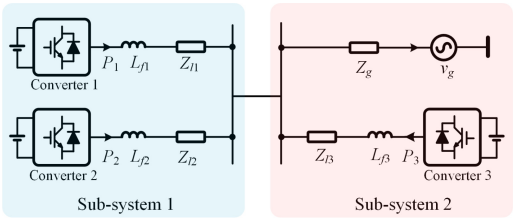

Fig. 8. Subsystem partitioning of Case 1.

TABLE I
PARAMETERS OF THREE CONVERTERS OF CASE 1-1 IN P.U.

Parameters	converter 1	converter 2	converter 3
P	0.33	0.33	0.33
α_c	10	6	8
α_a	0.2	0.04	0.75
α_f	15	30	20
G_{ad}	0.77	1.3	0.4
G_{aq}	0.77	1.3	0.4
K_p	0.9	0.54	0.72
K_q	0.15	0.15	0.15
K_v	0	0.27	0

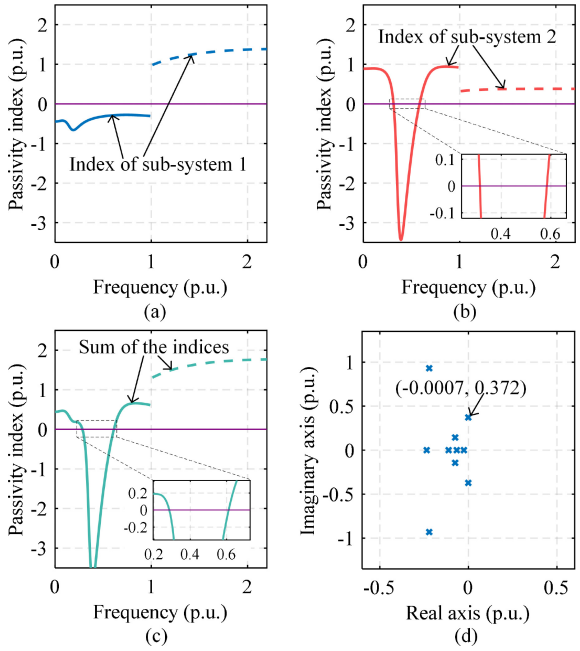

Fig. 9. Steps 1 to 5 for system diagnosis and risk assessment in Case 1-1. (a) Unified passivity index of sub-system 1. (b) Unified passivity index of sub-system 2. (c) Sum of the unified passivity index of sub-system 1 and sub-system 2. (d) Closed-loop system pole map before de-risking.

2 includes converter 3 and the grid, as shown in Fig. 8 where the line impedance is ignored for simplicity. The short circuit ratio (SCR) is 1.1, and the converter parameters are listed in Table I. It should be noted that α_f denotes the bandwidth of the first-order low-pass filters $H_1(s)$ and $H_2(s)$ shown in Fig. 7. This scenario is referred to as Case 1-1.

Fig. 9 presents the index plots and the pole-zero plot for Case 1-1. It is important to reiterate that the discontinuity in the index plot arises from the differing index definition methods across frequency ranges, as outlined in (18) and (19). In Fig. 9(a), the unified passivity index for Subsystem 1, representing $\mathbf{Y}_1 + \mathbf{Y}_2$, is shown. Fig. 9(b) shows the index

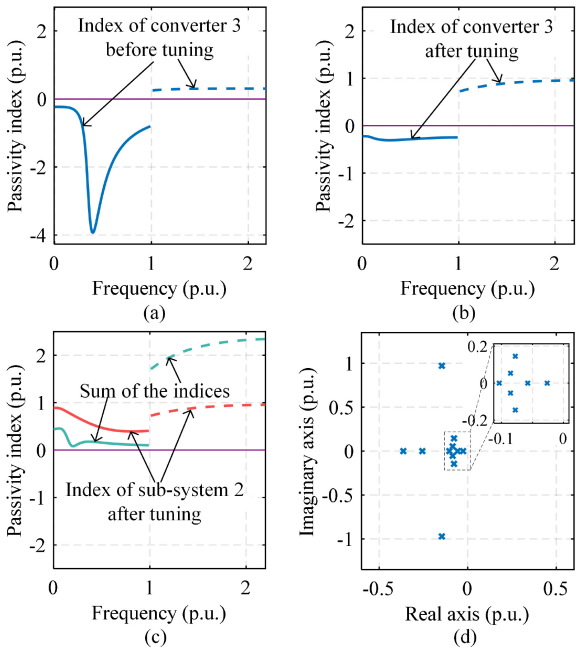

Fig. 10. Step 6 for system diagnosis and risk assessment in Case 1-1. (a) Unified passivity index of converter 3 before tuning. (b) Unified passivity index of converter 3 after tuning. (c) Sum of the unified passivity index of sub-system 1 and sub-system 2. (d) Closed-loop system pole map after de-risking.

plot for Subsystem 2, which includes the grid impedance and converter 3. Fig. 9(c) shows the sum of the indices for both subsystems. According to (25), if the sum in Fig. 9(c) is positive at all frequencies, the system is stable; if negative at certain frequencies, those bands suggest potential instability. From Figs. 9(a)-(c), it is evident that for frequencies above 1 p.u., both subsystems show positive indices, indicating no instability risk. However, at frequencies below 1 p.u., Fig. 9(c) reveals a negative peak between 0.3 and 0.6 p.u., indicating a significant risk of low-frequency resonance. Fig. 9(d), showing the closed-loop system pole plot, indicates critical stability, with a pair of poles near the imaginary axis at 0.372 p.u.

To mitigate this risk, the negative peak in Fig. 9(c) must be eliminated. By comparing the two subsystems, it is clear that the negative peak originates from Subsystem 2, as shown in its index plot in Fig. 9(b). Therefore, further diagnosis of Subsystem 2 is conducted, as shown in Fig. 10. Subsystem 2 consists of converter 3 and the grid impedance (repeated). Since the grid impedance provides excess passivity at low frequencies, the negative peak cannot be attributed to it; thus, converter 3 is identified as the source of the issue. Fig. 10(a) shows the index plot for converter 3, where a negative peak manifests. Eliminating this peak will reduce the resonance risk of the system. Fig. 10(b) presents the corresponding index plot of the re-tuned Converter 3 (G_{ad} and G_{aq} tuned to 1.38 p.u., α_a tuned to 0.072 p.u.), showing that the negative peak has been eliminated. Fig. 10(c) shows the unified passivity index plots for Subsystem 2 after being re-tuned and the summed indices for both subsystems (Subsystem 1 is not shown as its plot remains unchanged). The combined indices are now positive across both frequency bands (below and above 1.0 p.u.),

TABLE II
PARAMETERS OF THREE CONVERTERS OF CASE 1-2 IN P.U.

Parameters	converter 1	converter 2	converter 3
P	0.33	0.33	0.33
α_c	10	6	8
α_a	0.2	0.04	0.16
α_f	15	30	20
G_{ad}	0.77	1.3	1.25
G_{aq}	0.77	1.3	1.25
K_p	0.9	0.65	0.85
K_q	0.15	0.15	0.15
K_v	0.45	1.35	0.36

indicating that the system meets stability conditions in (25). Fig. 10(d) confirms that the resonance risk has been eliminated because the poles in the near-synchronous frequency range have moved away from the imaginary axis.

The second case study, denoted as Case 1-2, is presented to further demonstrate the proposed method using the same system configuration and subsystem partitioning as in Case 1-1 (Fig. 8). For this case, the parameters of the three converters are given in Table II, and the corresponding passivity index plots are shown in Fig. 11. From Fig. 11(a), it can be seen that the index plot of subsystem 1 exhibits two frequency bands where the index is negative—namely around $\omega = 0$ and $\omega = 1$. Fig. 11(b) shows that the index plot of subsystem 2 remains positive across all frequencies, which from a passivity perspective indicates that subsystem 2 is not destabilizing. Fig. 11(c) presents the sum of the two indices: the passivity deficiency of subsystem 1 near zero frequency is compensated by the excessive passivity of subsystem 2, but for $\omega > 1$ the sum is negative, signaling a potential oscillatory risk. The closed-loop pole–zero map in Fig. 11(d) confirms the presence of a pole very close to the imaginary axis, with the system on the verge of instability.

To eliminate the oscillations, it is necessary to restore passivity at frequencies above $\omega = 1$. As seen in Fig. 11(a), subsystem 1 (i.e., converter 1 and converter 2) presents a high risk. Figs. 12(a) and 12(b) show the individual index plots for converter 1 and converter 2, respectively. Converter 1 has a positive index in the high-risk band and can therefore be considered low risk, whereas Converter 2 exhibits a negative index in the band of interest and is the main culprit. Therefore, we adjust K_v of converter 2 from 1.35 p.u. to 0.54 p.u. Fig. 12(c) shows the plot of the sum of the indices of subsystem 1 and subsystem 2 after this readjustment. It can be seen that the negative region for $\omega > 1$ is eliminated, the stability condition is satisfied, and the risk is removed. The closed-loop pole–zero map in Fig. 12(d) also shows that the pole near 1 p.u. has shifted to the left.

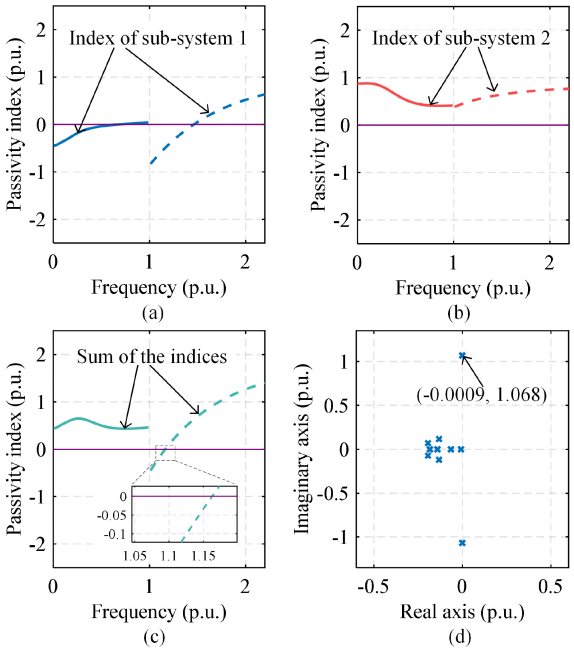

Fig. 11. Steps 1 to 5 for system diagnosis and risk assessment in Case 1-2. (a) Unified passivity index of sub-system 1. (b) Unified passivity index of sub-system 2. (c) Sum of the unified passivity index of sub-system 1 and sub-system 2. (d) Closed-loop system pole map before de-risking.

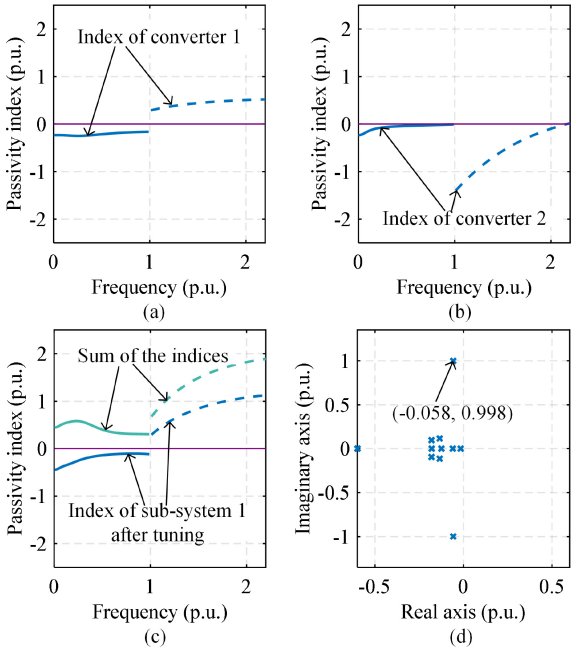

Fig. 12. Step 6 for system diagnosis and risk assessment in Case 1-2. (a) Unified passivity index of converter 1 before tuning. (b) Unified passivity index of converter 2 before tuning. (c) Sum of the unified passivity index of sub-system 1 and sub-system 2 after converter 2 is re-tuned. (d) Closed-loop system pole map after de-risking.

V. A FULLY LOCAL AND DECENTRALIZED SYSTEM DESIGN METHOD FOR MITIGATING SYSTEM OSCILLATION RISKS

In addition to the risk localization and mitigation methods mentioned in the previous section, another way to avoid oscillation risks in the system is to design the converters appropriately from the outset. When applying the passivity-based stability conditions in (20) or (22) to assess system stability, calculating or measuring the passivity index of each converter independently can help reduce information accumulation. However, this approach still cannot fully decouple the coupling between each converter and the grid impedance, as the overall system stability depends on the sum of these indices.

The main objective of this section is to propose a passivity-based design method for multi-converter systems that ensures system stability without needing to consider interactions between converters or between converters and the grid. With this approach, each converter only needs to meet its own local design reference to ensure system stability.

A. Local Passivity-Based Design

In high-frequency ranges, the unified passivity index of the grid impedance is zero. To avoid oscillations, the converter admittance should be designed to be dissipative. In low frequencies, according to [21], the unified passivity index of the inductive grid impedance is inherently non-negative. This surplus passivity can compensate for the passivity deficiency of a converter, making the passivity index of the grid a viable frequency-domain design reference for converters. By allocating the excess passivity of the grid proportionally based on the rated power of each converter $k_i(\sum_{i=1}^{N} k_i = 1)$, each converter can be assigned a non-negative $k_i\rho_E(\mathbf{Z}_g(s), \omega)$. Thus, considering the entire frequency range, to ensure system stability, it is required that each converter satisfies

$$\nu_E(\mathbf{Y}_i(s), \omega) + k_i\rho_E\big(\mathbf{Z}_{\mathrm{g}}(s), \omega\big) > 0, \ \forall\omega \in [0, \ +\infty]. \quad (26)$$

If each converter meets this condition, then it is guaranteed that the overarching inequality (22) is satisfied when summing across all converters. Notably, (26) offers a local passivity criterion for individual converters. Furthermore, as highlighted in [21], an increase in the SCR leads to a higher passivity index for the grid impedance in the low frequencies. Therefore, if the SCR of the grid is known during system design, it can be directly utilized. In scenarios where grid impedance details are absent, assuming an SCR of 1.1 can approximate the worst-case scenario, facilitating a conservative design. The proposed approach is summarized as follows:

Step 1: Check the grid impedance information:

- If the SCR is known, use the corresponding unified passivity index of grid impedance.
- If the SCR is unknown, simulate the worst-case scenario by using the passivity index when SCR=1.1.

Step 2: Distribute Excessive Passivity:

- Allocate the excess passivity of the grid impedance (positive at low frequencies and zero at high frequencies) to different converters based on their proportions of the total rated power.

Step 3: Passivity Index Tuning:

- Tune the passivity index for each converter to ensure that it meets the local stability condition (26).

B. Case Study

This numerical example is denoted as Case 2. Consider a system with three GFM converters, each active power rated at 0.33 p.u., and an SCR of 1.1. The control structure of the converters adopts the universal architecture proposed in [38], which is shown in Fig. 7. The parameters for the three converters are provided in Table II. According to the recommended steps, one-third of the grid impedance's passivity degree is allocated to converter 1. This allocation yields the local stability condition for converter 1, i.e., $k_1 = 1/3$

$$\nu_E(\mathbf{Y}_1(s), \omega) > \underbrace{-k_1\rho_E\big(\mathbf{Z}_{\mathrm{g}}(s), \omega\big)}_{\text{design reference}}. \quad (27)$$

The conditions for the remaining two converters are the same. In practical tuning, specific measures include adjusting the gains of the *P-f* droop and *Q-V* droop (with gains constrained by the operator and the converter own capacity), as well as tuning the inner loops, particularly the voltage control structure and parameters, and adjusting the active power output. The specific tuning methods are not the focus of this article and, therefore, will not be discussed in detail here. The parameters of the three converters and their corresponding index plots are shown in Fig. 13, where the blue curve represents $\nu_E(\mathbf{Y}_i(s), \omega)$, while the red reference curve represents $-k_i\rho_E(\mathbf{Z}_{\mathrm{g}}(s), \omega)$. The passivity index curves are distinguished by solid and dashed lines, which denote the low-frequency and high-frequency bands, respectively. Fig. 13(d) presents the pole-zero plot of the closed-loop system, demonstrating that the system is stable.

TABLE III
PARAMETERS OF THREE CONVERTERS OF CASE 2 IN P.U.

Parameters	converter 1	converter 2	converter 3
P	0.33	0.33	0.33
α_c	10	8	8
α_a	0.15	0.08	0.2
α_f	15	30	20
G_{ad}	0.77	1.4	0.83
G_{aq}	0.77	1.4	0.83
K_p	0.9	0.65	0.85
K_q	0.15	0.15	0.15
K_v	0.88	0.35	1.15

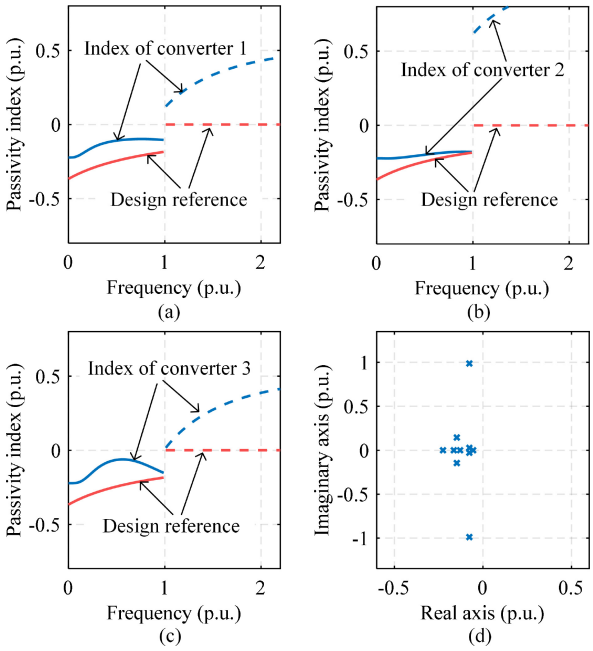

Fig. 13. Case 2. (a) Unified passivity index of converter 1 and corresponding design reference. (b) Unified passivity index of converter 2 and corresponding design reference. (c) Unified passivity index of converter 3 and corresponding design reference. (d) Closed-loop system pole map.

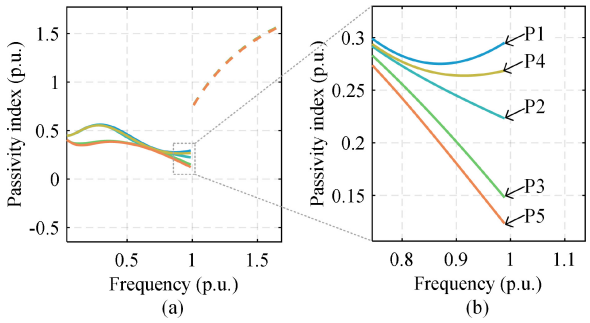

Fig. 14. Comparison of different system partitioning.

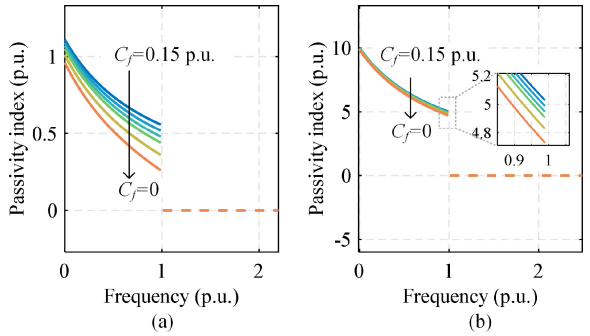

Fig. 15. Impact of filter capacitance. (a) SCR=1.1. (b) SCR=10.

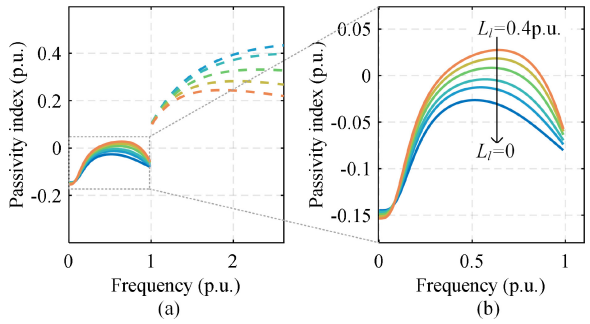

Fig. 16. Impact of line impedance.

VI. Discussions

This section examines the applicability of the proposed method, taking into account the effects of grid impedance, line impedance, converter operating conditions, and system partitioning. A comparative analysis with other existing methods is also provided.

A. Impact of System Partitioning

Equation (25) presents a *highly general* decentralized stability criterion that remains valid regardless of how the overall system is partitioned. In this subsection, we examine how different partitioning strategies affect the *conservativeness* of the proposed method. The three-converter system in Fig. 8 is reused, with each converter having the same parameters as in Case 2. Fig 14 compares the *sum of the stability indices* obtained under five alternative partitions, denoted P_1–P_5:

- P_1: The entire system is treated as a single plant (no partitioning);
- P_2: *converter* 1 and *converter* 2 form Subsystem 1, while *converter* 3 plus the grid impedance constitute Subsystem 2;
- P_3: *converters* 1–3 are grouped as Subsystem 1, and the grid impedance alone is Subsystem 2;
- P_4: *converter* 1 is Subsystem 1, whereas *converters* 2–3 together with the grid impedance make up Subsystem 2;
- P_5: *converter* 1, *converter* 2, *converter* 3, and the grid impedance are treated as four separate subsystems.

As shown in Fig. 14, the numerical results show that P_1 yields the *least conservative* condition (largest aggregate index), whereas P_5 is the *most conservative* (smallest aggregate index); the outcomes for P_2–P_4 lie in between. This agrees with the theoretical expectation in Section IV-A: analyzing the whole system as a single entity minimizes conservativeness, while treating every component as an individual subsystem maximizes it. Consequently, if the stability criterion is satisfied under the most conservative partition P_5, the system is guaranteed to be stable under *any* other partition. Therefore, condition (22) can be regarded as a recommended *robust* stability condition, independent of the chosen partition, albeit at the expense of maximal conservativeness.

B. Impact of Electrical Resonance and Line Impedance

In the preceding analysis, the filter capacitor (C_f) and the line impedance were neglected for simplicity. This subsection evaluates how the inclusion of these two elements affects the proposed method.

Filter capacitor lumped into the grid side. By assigning the filter capacitor to the grid-impedance branch, Fig. 15(a) and Fig. 15(b) show the grid-impedance passivity index when the capacitor varies from 0 to 0.15 p.u. for (i) SCR $=$ 1.1 ($L_g = 0.9$ p.u.) and (ii) SCR $=$ 10 ($L_g = 0.1$ p.u.), respectively. For $\omega > 1$, the presence of C_f has no impact on the index; within $0 < \omega < 1$, C_f slightly reduces the index, thereby increasing conservativeness. Given that practical filter capacitances are typically below 0.1 p.u. [38], their influence on the proposed criterion is negligible.

Line impedance included in the converter admittance. Fig. 16 depicts the converter admittance $\mathbf{Y}$ re-computed according to (3) as the line impedance increases from 0 to 0.4 p.u. Adding line impedance marginally lowers the index at low frequencies (around 0 p.u.), yet *raises* the passivity value at higher frequencies. Hence, line impedance does not significantly tighten the proposed stability condition; in fact, it reduces conservativeness over most of the frequency range.

C. Impact of Converter Operating Point

Using *converter 1* in Case 2 with fixed control parameters, Fig. 17 presents the passivity-index curves as the output power is swept from the rated value down to zero. It is evident that, with increasing output power, the passivity index drops in the low-frequency range; hence the *rated-power* condition represents the *worst case* for the converter index. In the previous examples, the system was therefore assessed, localized, and mitigated at this rated operating point via the proposed method.

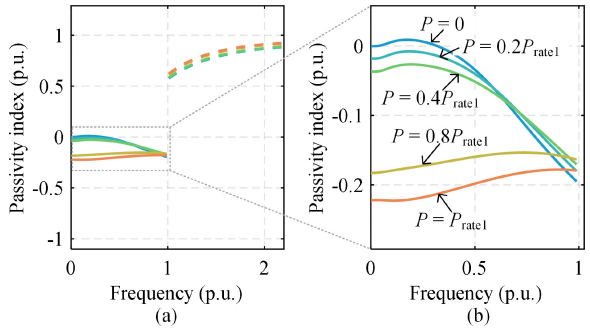

Fig. 17. Impact of operating point.

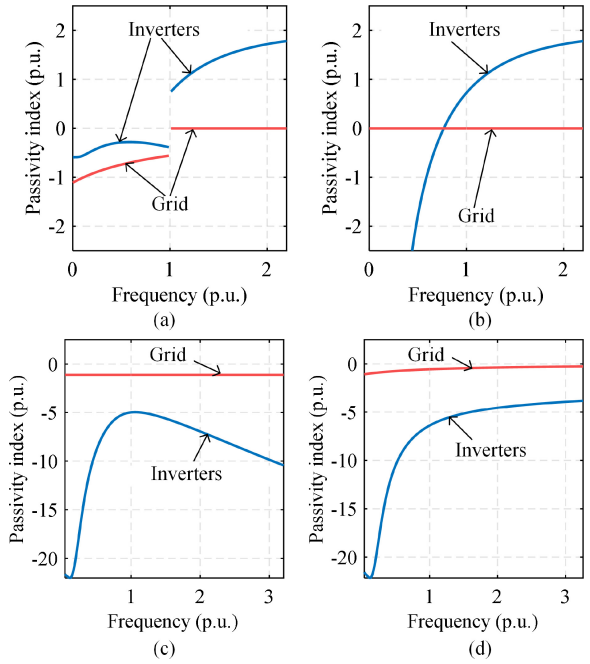

Fig. 18. Comparison of the proposed method with existing methods. (a) Proposed method, (b) Conventional passivity, (c) Weighted small-gain, (d) Conventional small-gain.

It must be emphasised that, once a subsystem is flagged as *risky*, the recommended mitigation strategy is *not* to reduce its output power, but rather to *retune the controller parameters* while maintaining rated power. On the other hand, if the analysis of a specific operating point is desired, the passivity index can be re-evaluated accordingly; reshaping the converter index by lowering the output power remains a viable option when appropriate.

D. Similarity and Difference Between Passivity Index Value and Phase Information

This subsection explores the relationship and distinction between the *passivity-index value* and *phase information*. We first revisit the conventional passivity concept for a SISO model. Let the converter admittance be denoted by $Y(j\omega)$. Passivity requires that, for all $\omega \in [0, \infty]$, the real part satisfies $\text{Re}\{Y(j\omega)\} > 0$, while no explicit constraint is imposed on the imaginary part $\text{Im}\{Y(j\omega)\}$. Consequently, for SISO systems,

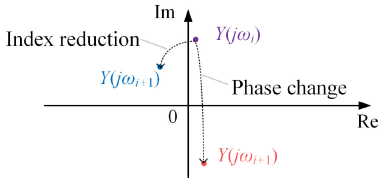

Fig. 19. Comparison between index value reduction and phase change.

the passivity condition can be re-expressed as: the phase of $Y(j\omega)$ must lie within $\pm 90°$.

However, a phase jump does *not* necessarily correspond to a meaningful change in the passivity index. Consider Fig. 19: let ω_i and ω_{i+1} be two adjacent frequency points. A 180° phase jump—from the purple segment to the red segment—may leave the real part almost unchanged. By contrast, the transition from the purple to the blue segment represents the passivity index crossing from positive to negative, yet the associated phase variation is clearly *not* 180°.

For MIMO systems the link between phase and index value becomes even weaker. We compute the real part of a matrix using the definition in (10) and interpret it conceptually as an analogue to the SISO real part. Moreover, the notion of "phase" for MIMO systems remains an emerging topic in the control-theory community [24]. Existing definitions often rely on *sectorality* conditions that the admittance matrices of power-electronic converters fail to satisfy, making them unfeasible for direct application in practical converter models [13]. Here, the stability criterion requires that the sum of all indices be positive. Consequently, a *negative* index value in the vicinity of the oscillation frequency is used to *identify the cause of instability*.

E. Numerical Comparison With Existing Decentralized Stability Criteria

Fig. 18 compares the proposed method with existing decentralized approaches. The converter parameters are chosen identically to those of converter 1 in Case 2. Note that the format in this figure is consistent with (27): the grid-side indicator serves as the reference for the converter-side indicator. Commonly used methods include passivity, small-gain [9], and phase approaches [24]; however, the phase method is new, and power-electronic systems do not satisfy the sectorial conditions required for phase-theory-based analysis, which warrants further investigation [13].

For clarity, Fig. 18 (a) reproduces Fig. 13(a), i.e., the proposed method. Fig. 18 (b) shows the conventional passivity index, which—due to the system's inherent non-dissipativity at low frequencies—cannot achieve full-frequency range stability specification. Fig. 18(c) and Fig. 18(d) depict the small-gain theorem, another common decentralized stability-analysis framework. The difference between Fig. 18 (c) and Fig. 18 (d) is that Fig. 18 (c) introduces a multiplier related to the grid impedance to reweight the subsystem dynamics (see [9] for details). For the closed-loop system $[\mathbf{Z}_g\ \mathbf{Y}]$, the small-gain stability condition requires $\bar{\sigma}(\mathbf{Z}_g(j\omega))\,\bar{\sigma}(\mathbf{Y}(j\omega)) < 1, \forall\,\omega$, where $\bar{\sigma}$ denotes the maximum singular value. To facilitate a more direct comparison with the proposed method, rewriting

this in the form of (27) yields the equivalent stability condition $-\bar{\sigma}(\mathbf{Y}(j\omega)) > -\frac{1}{\bar{\sigma}(\mathbf{Z}_g(j\omega))}, \forall \omega$. In the weighted gain-based approach, the expressions are identical to those of the conventional gain-based method, except that $\mathbf{Z}_g$ and $\mathbf{Y}$ are multiplied by the corresponding weighting multipliers. Although gain-based methods can in principle support stability assessment, localization, and mitigation, in practice—as discussed in [9], [13], [20], [39]—the small-gain criterion remains overly conservative, especially for GFM converter systems, making it difficult to directly apply gain-based stability indicators for full-frequency specification.

Modal analysis is a well-established system-diagnostic technique [40], [41]; however, its implementation differs fundamentally from the proposed passivity-based method. Modal analysis typically requires an explicit analytical model to compute the closed-loop system poles, followed by the calculation of participation factors for each subsystem to identify the "culprit" state variables. In contrast, the passivity-based approach developed here is applicable to both analytical and measured models: although the impedance modeling in this work employs analytical information, impedance data obtained through measurement can be directly used to calculate passivity index. Furthermore, the proposed method locates the risk frequency bands directly from the negative regions of each subsystem's passivity index plot and identifies the responsible subsystem by the magnitude of its negative index. This procedure is both simpler and more direct than first determining critical modes and then computing participation factors.

F. Applicability and Limitations

The proposed method focuses on risk assessment, localization, and mitigation of complex voltage–power coupling interactions in multi-GFM converter systems. Nevertheless, the theoretical framework applies to any MIMO interconnected feedback system [21], including conventional PLL-synchronized converters. In [21], the approach was validated on a single-converter, PLL-synchronized system with current control, a case not typically classified as GFM converters. For large-scale systems featuring both GFM and GFL converters, the proposed method remains fully compatible. In this study, the dc-side voltage is provided by a dc voltage source. This setup decouples the DC-side dynamics from the converter of interest; as a result, dc-side dynamics are not considered. However, since this work is based on passivity theory and impedance modeling, the impedance-modeling technique and passivity theory used here can fully incorporate dc-side dynamics [42]. Therefore, the proposed method can also be applied to scenarios with regulated dc-link dynamics.

In the authors' earlier work [19], classical passivity theory showed that a converter is *non-passive*—its behavior, particularly around $\omega = 0$ in the d–q frame, is inherently a power source. By introducing an extended passivity framework and an appropriate control design, this work demonstrates that, although the converter's index remains negative, stability specification is still possible. However, achieving a positive index for a converter across the *entire* spectrum is still unrealistic at present; from a passivity perspective, the grid impedance must contribute the remaining positive component to ensure stable low-frequency behavior. Hence, the proposed method is most suitable for *grid-connected* converter systems, where it enables complete risk assessment, localization, and mitigation.

For a 100% converter-based power system, the method can still assess and localize risks, but mitigation becomes difficult because satisfying the stability condition without any support from the local grid is excessively demanding. To the best of the authors' knowledge, no existing decentralized stability indicator guarantees system stability while ignoring the local grid [9], [13]. Further theoretical and analytical efforts on decentralized stability indicators for power-electronic-dominated systems are therefore needed.

TABLE IV
PARAMETERS OF THE EXPERIMENTAL PLATFORM AND THE CONTROLLERS

Parameters	Actual value (p.u.)
Rated power	2 kVA (1.0)
Rated voltage	110 V (1.0)
Rated current	8.57 A (1.0)
Based impedance	18.15 Ω (1.0)
Filter inductance L	5 mH (0.085)
Filter capacitance C	12.5 μF (0.075)
Grid impedance L_g	12.5 mH (0.22)
Fundamental frequency	50 Hz (1.0)
Switching frequency	10k Hz (200)
Bandwidth of CC	1000π rad/s (10.0)
α_f	800π rad/s (8.0)

VII. EXPERIMENTAL RESULTS

Experimental tests are conducted on a downscaled dual GFM converter system, as shown in Fig. 20. The two converters are labeled as VSC1 and VSC2, respectively. The basic system and controller parameters are listed. The control structures of the two converters are shown in Fig. 7, but the parameters differ, distinguished by subscripts 1 and 2. The system rated power is 2 kW, with each converter rated at 1 kW. The grid voltage base value is 110 V, and specific parameters and their p.u. values according to the system base are listed in Table IV. However, it is important to note that for ease of presentation, the p.u. values of the active power in the following experimental waveforms are shown based on the base value of a single converter.

Fig. 21 shows the waveform of stable operation. Initially, both converters operate at 0.1 p.u. power output and eventually at rated power (1.0 p.u.). Both converters adopt identical designs, and Figs. b and c show the passivity index (blue) plots and corresponding design references (red) at the operating points. The gain of α_a is set to 0.2 p.u., K_v is set to 0.55 p.u., K_p is set to 0.4 p.u., and K_q is set to 0.1 p.u., while all other parameter designs are consistent with those described in [38]. It can be seen that at different operating points, the converters satisfy the local passivity-based stability condition proposed in Section IV, leading to a stable system.

Fig. 22 presents the system waveform at rated power output. At 2s, the integrator gain of VSC2's voltage loop is increased from 0.2 p.u. to 0.5 p.u., while VSC1's design remains

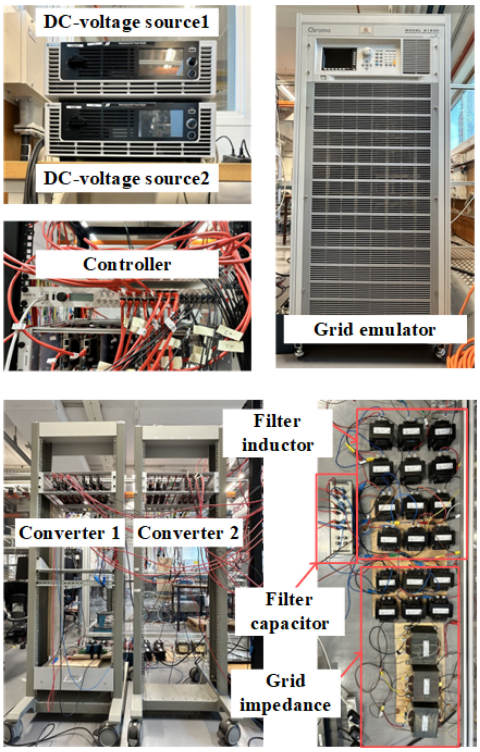

Fig. 20. Experimental platform.

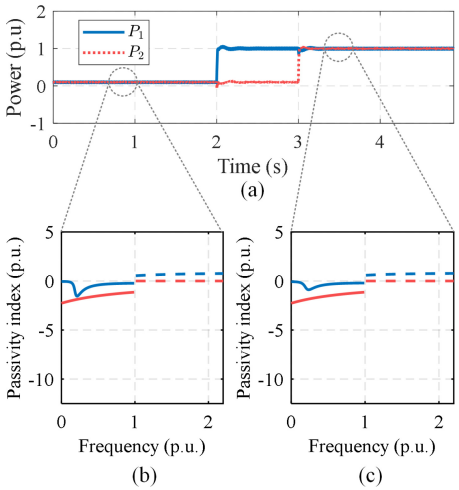

Fig. 21. Stable operation. (a) Waveform. (b) Index of the first operating point and design reference. (c) Index of the second operating point and design reference.

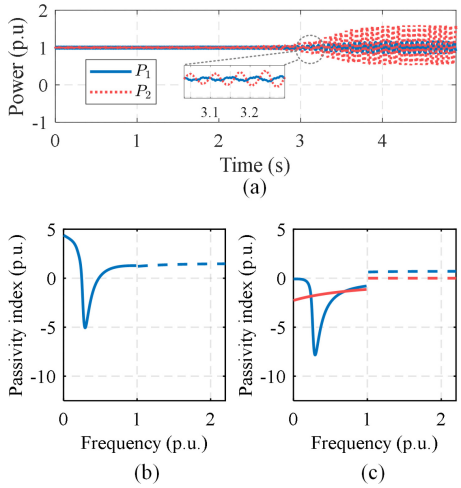

Fig. 22. Unstable operation. (a) Waveform. (b) Sum of the indices of VSC1, VSC2, and grid impedance. (c) Index of VSC2 and design reference.

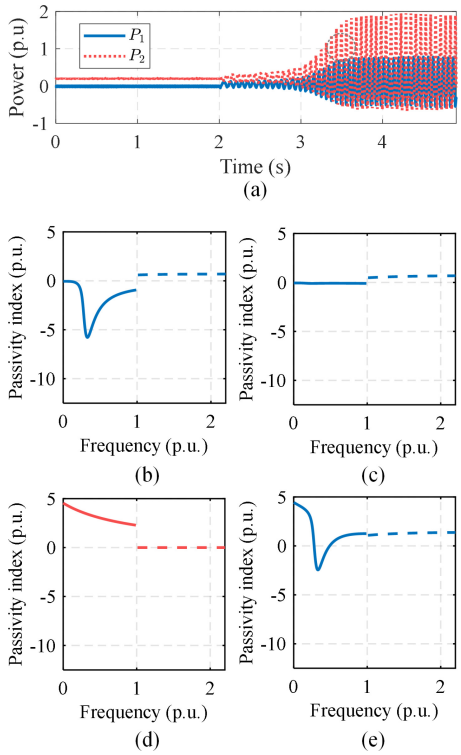

Fig. 23. Unstable waveform when VSC1 is connected to the grid. (a) Waveform. (b) Index of VSC2. (c) Index of VSC1. (d) Index of grid impedance. (e) Sum of the indices of two converters and grid impedance.

unchanged, causing system instability. Figs. b and c show the sum of the indices and VSC2's index plot, respectively. It can be observed that the system does not satisfy the stability condition proposed in equation (18), and VSC2 also fails to meet its local design reference. From the perspective of the passivity index plot, VSC2 represents a poor design. The experimental waveforms in Figs. 21 and 22 verify the effectiveness of the local passivity stability condition.

Fig. 23 presents the experiment on the interaction between a newly connected converter and the original system. Before 2 seconds, only VSC2 is connected to the grid, outputting 0.2 p.u. of power. After the second, when VSC1 is connected, the system oscillates. Figs. 23(b), 23(c), 23(d), and 23(e) show the plots of converter 2, converter 1, grid impedance, and the sum of the indices of the three subsystems, respectively. It can be seen that near the oscillation frequency, the sum of the indices is negative. Therefore, to stabilize the system, eliminating the negative values is needed. Next, the passivity index is used to assess which converter should be tuned. First, considering converter 1, its index is very close to zero in the low-frequency range. If VSC1's index is adjusted to make the sum of the indices in Fig. 23(d) positive across all frequency ranges, then converter 1 would need an index of approximately 3 in the

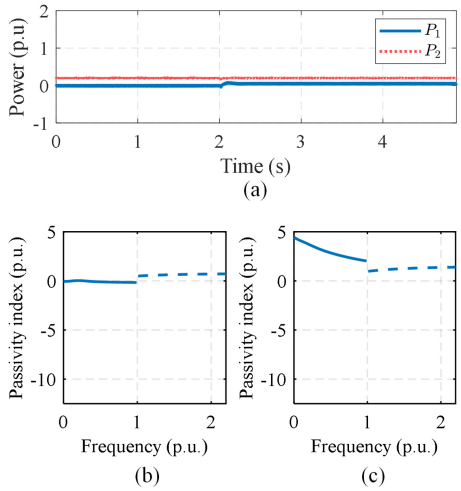

Fig. 24. Stable waveform when VSC1 is connected to the grid. (a) Index of VSC2 after being tuned. (b) Sum of the indices of two converters and grid impedance.

corresponding frequency range. In practice, this would be very difficult to achieve through tuning. Another option is to tune VSC2. From Fig. 23(b), it is clear that the system can be stabilized by increasing VSC2's minimum index value from -6 to around -3, meaning that tuning VSC2 is significantly less costly than tuning VSC1. Fig. 24(b) shows the index plots of converter 2 after adjustment. Fig. 24(c) shows the sum of the indices of converter 1, converter 2, and the grid impedance, from where it can be seen that the system is now stable. The experimental results in Fig. 24(a) also confirm the correctness of the theoretical analysis. Thus, when system oscillations occur, at least one subsystem is a "bad design," or the root cause of the oscillations, requiring retuning. The passivity index plot provides a clear means of quantifying the cost of adjusting a specific converter or subsystem to stabilize the system, allowing identification of the "bad design."

VIII. Conclusion

This article presents extended passivity–based methods for small-signal stability risk assessment, instability source localization, and mitigation in multi-parallel GFM converter systems. These methods include specially designed stability conditions and practical guidelines. Numerical and experimental results validate the effectiveness of the proposed approach, demonstrating streamlined implementation and reduced conservativeness. Future research may explore the impacts of different controller structures and parameter choices within the extended passivity framework, as well as applications to more complex power-electronic systems.

References

[1] C. Yang, L. Huang, H. Xin, and P. Ju, "Placing grid-forming converters to enhance small signal stability of PLL-integrated power systems," *IEEE Trans. Power Syst.*, vol. 36, no. 4, pp. 3563–3573, Jul. 2021.

[2] V. Häberle, A. Tayyebi, X. He, E. Prieto-Araujo, and F. Dörfler, "Grid-forming and spatially distributed control design of dynamic virtual power plants," *IEEE Trans. Smart Grid*, vol. 15, no. 2, pp. 1761–1777, Mar. 2024.

[3] A. Singhal, T. L. Vu, and W. Du, "Consensus control for coordinating grid-forming and grid-following inverters in microgrids," *IEEE Trans. Smart Grid*, vol. 13, no. 5, pp. 4123–4133, Sep. 2022.

[4] Q. Hu et al., "Grid-forming inverter enabled virtual power plants with inertia support capability," *IEEE Trans. Smart Grid*, vol. 13, no. 5, pp. 4134–4143, Sep. 2022.

[5] A. Elnady, A. A. A. Ismail, M. AlShabi, and A. Noureldin, "A comprehensive review of centralized current/power control schemes for parallel inverters and AC microgrids," *IEEE Access*, vol. 10, pp. 125061–125085, 2022.

[6] S. Jiang and G. Konstantinou, "Generalized impedance model and interaction analysis for multiple grid-forming and grid-following converters," *Electr. Power Syst. Res.*, vol. 214, Jan. 2023, Art. no. 108912.

[7] F. Cavazzana, T. Caldognetto, P. Mattavelli, M. Corradin, and I. Toigo, "Analysis of current control interaction of multiple parallel grid-connected inverters," *IEEE Trans. Sustain. Energy*, vol. 9, no. 4, pp. 1740–1749, Oct. 2018.

[8] S. Liao, Y. Chen, W. Wu, L. Wang, and Q. Xu, "Closed-loop interconnected model of multi-inverter-paralleled system and its application to impact assessment of interactions on damping characteristics," *IEEE Trans. Smart Grid*, vol. 14, no. 1, pp. 41–53, Jan. 2023.

[9] L. Huang et al., "Gain and phase: Decentralized stability conditions for power electronics-dominated power systems," *IEEE Trans. Power Syst.*, vol. 39, no. 6, pp. 7240–7256, Nov. 2024.

[10] A. Gonzalez-Cajigas, J. Roldán-Pérez, and E. J. Bueno, "Design and analysis of parallel-connected grid-forming virtual synchronous machines for island and grid-connected applications," *IEEE Trans. Power Electron.*, vol. 37, no. 5, pp. 5107–5121, May 2021.

[11] S. Wang, Z. Liu, J. Liu, D. Boroyevich, and R. Burgos, "Small-signal modeling and stability prediction of parallel droop-controlled inverters based on terminal characteristics of individual inverters," *IEEE Trans. Power Electron.*, vol. 35, no. 1, pp. 1045–1063, Jan. 2020.

[12] L. Harnefors, X. Wang, A. G. Yepes, and F. Blaabjerg, "Passivity-based stability assessment of grid-connected VSCs—An overview," *IEEE Trans. Emerg. Sel. Topics Power Electron.*, vol. 4, no. 1, pp. 116–125, Mar. 2015.

[13] L. Woolcock and R. Schmid, "Mixed gain/phase robustness criterion for structured perturbations with an application to power system stability," *IEEE Control Syst. Lett.*, vol. 7, pp. 3193–3198, 2023.

[14] L. Huang, H. Xin, and F. Dörfler, "H^∞-control of grid-connected converters: Design, objectives and decentralized stability certificates," *IEEE Trans. Smart Grid*, vol. 11, no. 5, pp. 3805–3816, Sep. 2020.

[15] Q. Chen, S. Bu, and C. Y. Chung, "Small-signal stability criteria in power electronics-dominated power systems: A comparative review," *J. Mod. Power Syst. Clean Energy*, vol. 12, no. 4, pp. 1003–1018, Jul. 2024.

[16] K. Dey and A. Kulkarni, "Passivity-based decentralized criteria for small-signal stability of power systems with converter-interfaced generation," *IEEE Trans. Power Syst.*, vol. 38, no. 3, pp. 2820–2833, May 2023.

[17] Y. Liao, X. Wang, and X. Wang, "Frequency-domain participation analysis for electronic power systems," *IEEE Trans. Power Electron.*, vol. 37, no. 3, pp. 2531–2537, Mar. 2022.

[18] L. Harnefors, M. Bongiorno, and S. Lundberg, "Input-admittance calculation and shaping for controlled voltage-source converters," *IEEE Trans. Ind. Electron.*, vol. 54, no. 6, pp. 3323–3334, Dec. 2007.

[19] F. Chen et al., "Limitations of using passivity index to Analyze grid–inverter interactions," *IEEE Trans. Power Electron.*, vol. 39, no. 11, pp. 14465–14477, Nov. 2024.

[20] Y. Song and C. Breitholtz, "VSC-HVDC system robust stability analysis based on a modified mixed small gain and passivity theorem," *IFAC-PapersOnLine*, vol. 50, no. 1, pp. 13–18, 2017.

[21] F. Chen et al., "An extended frequency-domain passivity theory for MIMO dynamics specifications of voltage-source inverters," *IEEE Trans. Power Electron.*, vol. 40, no. 2, pp. 2943–2957, Feb. 2025.

[22] F. Zhao, T. Zhu, Z. Li, and X. Wang, "Low-frequency resonances in grid-forming converters: Causes and damping control," *IEEE Trans. Power Electron.*, vol. 39, no. 11, pp. 14430–14447, Nov. 2024.

[23] W. Chen, D. Wang, S. Z. Khong, and L. Qiu, "A phase theory of multi-input-multi-output linear time-invariant systems," *SIAM J. Control Optim.*, vol. 62, no. 2, pp. 1235–1260, 2024.

[24] D. Wang, W. Chen, and L. Qiu, "The first five years of a phase theory for complex systems and networks," *IEEE/CAA J. Automatica Sinica*, vol. 11, no. 8, pp. 1728–1743, Aug. 2024.

[25] S. Z. Khong, "Feedback stability of generalised positive real and negative imaginary systems," *IEEE Trans. Autom. Control*, vol. 68, no. 10, pp. 6285–6290, Oct. 2022.

[26] S. Z. Khong and A. Lanzon, "Feedback stability analysis via frequency dependent constraints," *IEEE Trans. Autom. Control*, vol. 70, no. 2, pp. 1228–1235, Feb. 2025.
[27] R. Pates and E. Mallada, "Robust scale-free synthesis for frequency control in power systems," *IEEE Trans. Control Netw. Syst.*, vol. 6, no. 3, pp. 1174–1184, Sep. 2019.
[28] F. Zhao et al., "Closed-form solutions for grid-forming converters: A design-oriented study," *IEEE Open J. Power Electron.*, vol. 5, pp. 186–200, Jan. 2024.
[29] F. Zhao et al., "A general integration method for small-signal stability analysis of grid-forming converter connecting to power system," in *Proc. IEEE 21st Workshop Control Model. Power Electron. (COMPEL)*, 2020, pp. 1–7.
[30] F. Chen, L. Zhao, L. Harnefors, J. Kukkola, M. Routimo, and X. Wang, "Dynamics enhancement for power Synchronization control with asymmetric AC voltage controller in strong grids," in *Proc. IEEE Conf. Control Technol. Appl. (CCTA)*, 2023, pp. 1066–1070.
[31] F. Chen, L. Zhao, L. Harnefors, and X. Wang, "Impedance modeling for quadrature-axis active damping of PLL dynamics," in *Proc. IEEE 23rd Workshop Control Model. Power Electron. (COMPEL)*, 2022, pp. 1–7.
[32] J. M. Uudrill, "Dynamic stability calculations for an arbitrary number of interconnected synchronous machines," *IEEE Trans. Power Appar. Syst.*, vol. PAS-87, no. 3, pp. 835–844, Mar. 1968.
[33] S. Skogestad and I. Postlethwaite, *Multivariable Feedback Control: Analysis and Design*. Hoboken, NJ, USA: Wiley, 2005.
[34] J. Bao, P. L. Lee, and B. E. Ydstie, *Process Control: The Passive Systems Approach*, London, U.K.: Springer, 2007.
[35] (ESIG, Reston, VA, USA). *Diagnosis and Mitigation of Observed Oscillations in IBR-Dominant Power Systems: A Practical Guide*. (2024). [Online]. Available: https://www.esig.energy/oscillations-guide/,
[36] W. M. Griggs, S. S. K. Sajja, B. D. O. Anderson, and R. N. Shorten, "On interconnections of 'mixed' systems using classical stability theory," *Syst. Control Lett.*, vol. 61, no. 5, pp. 676–682, 2012.
[37] S. Z. Khong, "On integral quadratic constraints," *IEEE Trans. Autom. Control*, vol. 67, no. 3, pp. 1603–1608, Mar. 2022.
[38] L. Harnefors, J. Kukkola, M. Routimo, M. Hinkkanen, and X. Wang, "A universal controller for grid-connected voltage-source converters," *IEEE Trans. Emerg. Sel. Topics Power Electron.*, vol. 9, no. 5, pp. 5761–5770, Oct. 2021.
[39] F. Chen, S. Z. Khong, X. Wang, and L. Harnefors, "Unified and flexible frequency-domain stability assessment framework for power-electronic-based power systems," *IEEE Trans. Power Electron.*, vol. 40, no. 10, pp. 14307–14312, Oct. 2025.
[40] P. Kundur, *Power System Stability and Control*. New York, NY, USA: McGraw-Hill, 1994.
[41] G. C. Verghese, I. J. Perez-Arriaga, and F. C. Schweppe, "Selective modal analysis with applications to electric power systems, Part II: The dynamic stability problem," *IEEE Trans. Power Appar. Syst.*, vol. PAS-101, no. 9, pp. 3126–3134, Sep. 1982.
[42] L. Zhao, X. Wang, and Z. Jin, "Impedance-based dynamics analysis for DC-link voltage-Synchronized voltage-source converters," *IEEE Trans. Power Electron.*, vol. 38, no. 9, pp. 10829–10844, Sep. 2023.

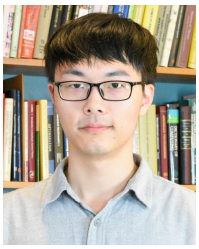

Feifan Chen (Member, IEEE) received the B.S. and M.S. degrees in electrical engineering from the Harbin Institute of Technology, Harbin, China, in 2019 and 2021, respectively, and the Ph.D. degree in electrical engineering from the School of Electrical Engineering and Computer Science, KTH Royal Institute of Technology, Stockholm, Sweden, in 2025. His research interests include modeling and control of grid-connected converters, stability assessment, dynamic analysis of power-electronic-dominated power systems, and motor drives.

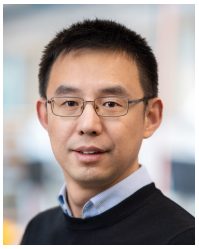

Xiongfei Wang (Fellow, IEEE) received the B.S. degree in electrical engineering from Yanshan University, China, in 2006, the M.S. degree in electrical engineering from the Harbin Institute of Technology, China, in 2008, and the Ph.D. degree in energy technology from Aalborg University, Denmark, in 2013. From 2009 to 2022, he was with Aalborg University, where he became an Assistant Professor in 2014, an Associate Professor in 2016, a Professor and the Founding Leader of Electronic Power Grid Research Group, in 2018. From 2022 to 2025, he was Professor with the KTH Royal Institute of Technology, Stockholm, Sweden, and a part-time Professor with Aalborg University. He is currently the Xinghua Chair Professor with Tsinghua University, Beijing, China. His research interests include modeling and control of power electronic converters, stability and power quality of power-electronic-dominated power systems, and high-power electronic systems.

Dr. Wang received 11 IEEE Prize Paper Awards, the 2016 AAU Talent for Future Research Leaders, the 2018 IEEE Richard M. Bass Outstanding Young Power Electronics Engineer Award, the 2019 IEEE PELS Sustainable Energy Systems Technical Achievement Award, and the 2022 Isao Takahashi Power Electronics Award. He serves as the Editor-in-Chief for the IEEE TRANSACTIONS ON POWER ELECTRONICS, and the Chair for IEEE International Roadmap on High-Power Electronics for Modern Energy Grids and IEEE Power Electronics Society Technical Committee (TC 8) on Electronic Power Grid Systems.

Lennart Harnefors (Fellow, IEEE) received the M.Sc., Licentiate, and Ph.D. degrees in electrical engineering from the Royal Institute of Technology (KTH), Stockholm, Sweden, in 1993, 1995, and 1997, respectively, and the Docent (D.Sc.) degree in industrial automation from Lund University, Lund, Sweden, in 2000. From 1994 to 2005, he was with Mälardalen University, Västerås, Sweden, from 2001 as a Professor of Electrical Engineering. From 2001 to 2005, he was, in addition, a part-time Visiting Professor of Electrical Drives with the Chalmers University of Technology, Göteborg, Sweden. In 2005, he joined ABB, HVDC Product Group, Ludvika, Sweden, where, among other duties, he led the control development of the first generation of multilevel-converter HVDC Light. In 2012, he joined ABB, Corporate Research, Västerås, where he was appointed as a Senior Principal Scientist in 2013 and as a Corporate Research Fellow in 2021. His research interests include control and dynamic analysis of power electronic systems, particularly grid-connected converters, and ac drives. He is, in addition, a part-time Visiting Professor with Aalto University, Espoo, Finland. He was the recipient of the 2020 IEEE Modeling and Control Technical Achievement Award. He is an Editor of the IEEE JOURNAL OF EMERGING AND SELECTED TOPICS IN POWER ELECTRONICS.

Sei Zhen Khong (Senior member, IEEE) received the Bachelor of Electrical Engineering degree (with first class hons.) and the Ph.D. degree in electrical engineering from the University of Melbourne, Australia, in 2008 and 2012, respectively. He held research positions with the Department of Electrical and Electronic Engineering, University of Melbourne, Australia, the Department of Automatic Control, Lund University, Sweden, the Institute for Mathematics and its Applications, University of Minnesota Twin Cities, USA, and the Department of Electrical and Electronic Engineering, University of Hong Kong, China. He is currently with the Department of Electrical Engineering, National Sun Yat-sen University, Taiwan. His research interests include network control, systems theory, and optimization with applications to systems biology, power systems, and electromechanical systems.

Jarno Kukkola received the B.Sc. (Tech.), M.Sc. (Tech.), and D.Sc. (Tech.) degrees in electrical engineering from the Aalto University, Espoo, Finland, in 2010, 2012, and 2017, respectively. He is currently an Research and Development Principal Engineer with ABB Oy Drives, Helsinki, Finland. His research interests include control systems and grid-connected converters.

Mikko Routimo (Member, IEEE) received the M.Sc. (El. Eng.), Lic.Tech., and D.Sc. (Tech.) degrees in electrical engineering from the Tampere University of Technology, Tampere, Finland, in 2002, 2005, and 2009, respectively. He joined ABB Oy Drives, Helsinki, Finland, in 2008, where he was appointed as a Senior Principal Engineer in 2022. From 2017 to 2022 he was, in addition, a part-time Professor of Practice with the School of Electrical Engineering, Aalto University, Espoo, Finland. His research interests include control of grid-connected converters and power electronics in power systems.

Liang Zhao (Member, IEEE) received the B.S. and M.S. degrees in electrical engineering from the Harbin Institute of Technology, Harbin, China, in 2018 and 2020, respectively, and the Ph.D. degree in power electronic systems from the Department of Energy, Aalborg University, Aalborg, Denmark, in 2024. He is currently a Postdoctoral Researcher with the KTH Royal Institute of Technology, Stockholm, Sweden. His research interests include modeling and control of power electronic converters and systems. He was the recipient of the best paper award for 2023 Wind and Solar Integration Workshop.

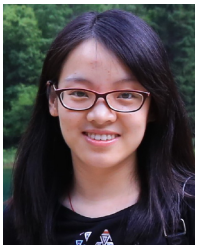

Dan Wang (Member, IEEE) received the B.S. degree in automation from the Hangzhou Dianzi University, Hangzhou, Zhejiang, China, in 2014, an the M.Phil. and Ph.D. degrees in electronic and computer engineering from The Hong Kong University of Science and Technology, Hong Kong, SAR, China, in 2016 and 2020, respectively. She is currently an Assistant Professor with the School of Robotics and Automation, Nanjing University. Prior to joining Nanjing University, she worked with the KTH Royal Institute of Technology and The Hong Kong University of Science and Technology for postdoctoral research. From January 2018 to July 2018, she was a Visiting Scholar with the University of Illinois at Urbana Champaign, Urbana, IL, USA. Her research interests include systems and control theory, phase theory, dynamical networks, renewable power systems, and control of epidemics.

Henrik Sandberg (Fellow, IEEE) received the M.Sc. degree in engineering physics and the Ph.D. degree in automatic control from Lund University, Lund, Sweden, in 1999 and 2004, respectively. He is Professor with the Division of Decision and Control Systems, KTH Royal Institute of Technology, Stockholm, Sweden. From 2005 to 2007, he was a Postdoctoral Scholar with the California Institute of Technology, Pasadena, USA. In 2013, he was a Visiting Scholar with the Laboratory for Information and Decision Systems, MIT, Cambridge, USA. He has also held visiting appointments with the Australian National University and the University of Melbourne, Australia. His current research interests include security of cyber–physical systems, power systems, model reduction, and fundamental limitations in control. He was a recipient of the Best Student Paper Award from the IEEE Conference on Decision and Control in 2004, the Ingvar Carlsson Award from the Swedish Foundation for Strategic Research in 2007, and the Consolidator Grant from the Swedish Research Council in 2016. He has served on the editorial boards of IEEE TRANSACTIONS ON AUTOMATIC CONTROL and the *IFAC Journal Automatica*.

Kin Cheong Sou (Member, IEEE) received the Ph.D. degree in electrical engineering and computer science with the Massachusetts Institute of Technology in 2008. From 2008 to 2010 he was a Postdoctoral Researcher with Lund University, Lund, Sweden. From 2010 to 2012 he was a Postdoctoral Researcher with the KTH Royal Institute of Technology, Stockholm, Sweden. From 2013 to 2016 he was an Assistant professor with the Department of Mathematical Sciences, Chalmers University of Technology and the University of Gothenburg, Sweden. He is currently an Associate Professor with the Department of Electrical Engineering, National Sun Yat-sen University, Taiwan. His research interests include decision-making and computation techniques for power systems applications.

Karl Henrik Johansson (Fellow, IEEE) received the M.Sc. degree in electrical engineering and the Ph.D. degree in automatic control from Lund University. He is Swedish Research Council Distinguished Professor in Electrical Engineering and Computer Science with the KTH Royal Institute of Technology, Sweden, and the Founding Director of Digital Futures. He has held visiting positions with UC Berkeley, Caltech, NTU, and other prestigious institutions. His research interests focus on networked control systems and cyber–physical systems with applications in transportation, energy, and automation networks. For his scientific contributions, he has received numerous best paper awards and various distinctions from IEEE, IFAC, and other organizations. He has been awarded the Distinguished Professor by the Swedish Research Council, the Wallenberg Scholar by the Knut and Alice Wallenberg Foundation, the Future Research Leader by the Swedish Foundation for Strategic Research. He has also received the triennial IFAC Young Author Prize and the IEEE CSS Distinguished Lecturer. He is the recipient of the 2024 IEEE CSS Hendrik W. Bode Lecture Prize. His extensive service to the academic community includes being the President of the European Control Association, IEEE CSS Vice President Diversity, Outreach & Development, and a member of IEEE CSS Board of Governors and IFAC Council. He has served on the editorial boards of *Automatica*, IEEE TRANSACTIONS ON AUTOMATIC CONTROL, and IEEE TRANSACTIONS ON CONTROL OF NETWORK SYSTEMS. He has also been a member of the Swedish Scientific Council for Natural Sciences and Engineering Sciences. He is Fellow of the Royal Swedish Academy of Engineering Sciences.